RESEARCH ARTICLE | JULY 02 2024

Theoretical description of photoinduced electron transfer in donor–acceptor supramolecular complexes based on carbon buckybowls

Raquel Rubert-Albiol ; Jesús Cerdá ; Joaquín Calbo ; Lorenzo Cupellini ; Enrique Ortí ; Juan Aragó

J. Chem. Phys. 161, 014304 (2024)
https://doi.org/10.1063/5.0215339

The Journal of Chemical Physics ARTICLE pubs.aip.org/aip/jcp

Theoretical description of photoinduced electron transfer in donor–acceptor supramolecular complexes based on carbon buckybowls

Cite as: J. Chem. Phys. 161, 014304 (2024); doi: 10.1063/5.0215339
Submitted: 23 April 2024 • Accepted: 10 June 2024 •
Published Online: 2 July 2024

Raquel Rubert-Albiol,[1] Jesús Cerdá,[1,2] Joaquín Calbo,[1] Lorenzo Cupellini,[3] Enrique Ortí,[1,a)] and Juan Aragó[1,a)]

AFFILIATIONS

[1] Instituto de Ciencia Molecular (ICMol), Universitat de València, Paterna 46980, Spain
[2] Laboratory for Chemistry of Novel Materials, Université de Mons, Mons 7000, Belgium
[3] Dipartimento di Chimica e Chimica Industriale, University of Pisa, Pisa, Italy

[a)] **Authors to whom correspondence should be addressed:** enrique.orti@uv.es and juan.arago@uv.es

ABSTRACT

Herein, we explore, from a theoretical perspective, the nonradiative photoinduced processes (charge separation and energy transfer) within a family of donor–acceptor supramolecular complexes based on the electron-donor truxene-tetrathiafulvalene (truxTTF) derivative and a series of curved fullerene fragments (buckybowls) of different shapes and sizes ($C_{30}H_{12}$, $C_{32}H_{12}$, and $C_{38}H_{14}$) as electron acceptors that successfully combine with truxTTF via non-covalent interactions. The resulting supramolecular complexes (truxTTF·$C_{30}H_{12}$, truxTTF·$C_{32}H_{12}$, and truxTTF·$C_{38}H_{14}$) undergo charge-separation processes upon photoexcitation through charge-transfer states involving the donor and acceptor units. Despite the not so different size of the buckybowls, they present noticeable differences in the charge-separation efficiency owing to a complex decay post-photoexcitation mechanism involving several low-lying excited states of different natures (local and charge-transfer excitations), all closely spaced in energy. In this intricate scenario, we have adopted a theoretical approach combining electronic structure calculations at (time-dependent) density functional theory, a multistate multifragment diabatization method, the Marcus–Levitch–Jortner semiclassical rate expression, and a kinetic model to estimate the charge separation rate constants of the supramolecular heterodimers. Our outcomes highlight that the efficiency of the photoinduced charge-separation process increases with the extension of the buckybowl backbone. The supramolecular heterodimer with the largest buckybowl (truxTTF·$C_{38}H_{14}$) displays multiple and efficient electron-transfer pathways, providing a global photoinduced charge separation in the ultrafast time scale in line with the experimental findings. The study reported indicates that modifications in the shape and size of buckybowl systems can give rise to attractive novel acceptors for potential photovoltaic applications.

INTRODUCTION

Photoinduced electron transfer (PET) is a key process in chemistry, biology, and materials science.[1] In archetype donor–acceptor (D–A) supramolecular complexes, PET takes place after a sequence of primary steps (Fig. 1). Initially, the electron-donor molecule generally absorbs a photon, generating an early excited state of local-type character (D^*–A).[2] Within this excited state, a favorable charge separation (CS)—i.e., an electron transfer from the donor molecule to the electron-acceptor moiety—occurs in a relatively fast timescale. Consequently, the donor molecule becomes positively charged, having lost an electron, while the acceptor molecule becomes negatively charged, having gained an electron, thus forming a charge-separated D^+–A^- state.[3–5] PET plays a crucial role in several technological applications, such as fluorescent sensors for detection, imaging and disease diagnosis,[6–8] artificial photosynthesis,[9,10] and photovoltaic devices.[11–14]

In the context of organic solar cells (OSCs), identifying molecular materials exhibiting efficient photoinduced CS processes is essential as an initial requirement before implementation in photovoltaic devices.[5,15] OSCs are typically structured as donor–acceptor heterostructures with a donating hole-conducting layer

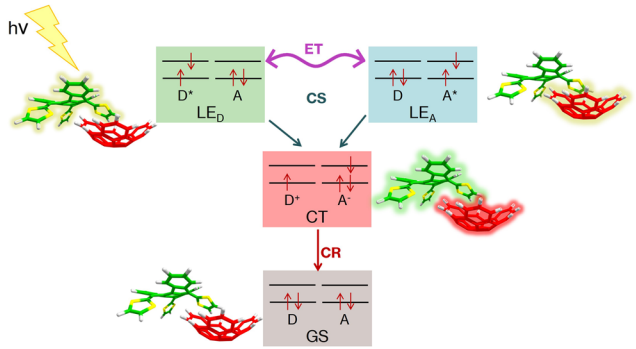

FIG. 1. Schematic representation of the charge-separation (CS), energy-transfer (ET), and charge-recombination (CR) photophysical processes taking place in donor–acceptor supramolecular complexes after photoexcitation. LE, CT, and GS stand for local excited, charge transfer, and ground electronic states, respectively.

and an accepting electron-conducting counterpart.[16,17] Fullerene derivates have become the dominant acceptors in this field owing to their excellent electron-transporting properties and favorable heterojunction morphology when combined with polymer donors.[18,19] For instance, efficient bulk heterojunctions result from a combination of a conjugated polymer (e.g., TQ1 or P3HT) as electron-rich donor systems[20–22] and fullerene derivatives as electron-deficient acceptor systems (PC61BM and PC71BM).[19,21,23–25] Over the last few years, OSCs based on non-fullerene acceptors (NFAs) have gained prominence owing to the significant increase in power conversion efficiency.[26] Among these NFAs, derivatives of perylene diimides (PDIs) with high photochemical stability,[27] IT-4F,[28] and Y6[14,29] exhibit favored charge-separation and transport characteristics.

Apart from NFAs, a novel category of fullerene fragments, termed buckybowls owing to their curved bowl-shaped structure, has been synthesized, giving rise to a family of electron acceptors of different sizes and curvatures.[30–34] Among this family, the $C_{30}H_{12}$, $C_{32}H_{12}$, and $C_{38}H_{14}$ buckybowls shown in Fig. 2 have been shown to mimic the photoinduced electron-accepting behavior of C_{60}. They successfully combine through non-covalent interactions with the electron-donor truxene-tetrathiafulvalene (truxTTF)[35] derivative, and the resulting supramolecular D–A complexes exhibit efficient photoinduced CS processes followed by slower charge-recombination (CR) events, making them potential candidates for OSCs.[36,37] However, despite the structural similarity of the buckybowl acceptor, important differences are found between the charge-separation rates reported for the three D–A complexes.[35,38–40] These differences motivated us to carry out a comprehensive and detailed analysis at the molecular level to fully understand the photoinduced charge-transfer properties of these buckybowls as a function of their size and shape. This knowledge can be useful for the design of not only enhanced buckybowl-based acceptors but also other types of novel non-fullerene acceptors for OSC applications.

In this study, we seek to gain insight into the kinetics of the nonradiative photoinduced processes [CS and energy transfer (ET)] experimented in solution by a family of D–A supramolecular complexes (truxTTF·$C_{30}H_{12}$, truxTTF·$C_{32}H_{12}$, and truxTTF·$C_{38}H_{14}$), in which the donor is the truxTTF molecule and the acceptors are the buckybowls $C_{30}H_{12}$, $C_{32}H_{12}$, and $C_{38}H_{14}$ (Fig. 2). Our primary objective is to establish meaningful structure–property relationships that may contribute to a more rational design of novel acceptors. To achieve this, we have adopted a computational protocol to accurately estimate the charge-separation in donor–acceptor (D–A) supramolecular assemblies in solution based on a previous study performed in our group.[41] Our approximation combines the Marcus–Levitch–Jortner (MLJ) semiclassical rate expression,[42,43] a multistate multifragment diabatization method, and state-of-the-art electronic structure calculations at the density functional theory (DFT) level to evaluate the key parameters of the rate expression, including properly the solvent polarization of the electronic excited states. Finally, all the results collected are merged into a kinetic model that combines the different non-radiative deactivation pathways, providing global rate constants comparable to those measured experimentally.

METHODOLOGY

Rate constant expression

To estimate the photoinduced electron-transfer events in buckybowl-based donor–acceptor supramolecular complexes, we used the Marcus–Levitch–Jortner (MLJ) electron-transfer rate expression,

$$k_{ij} = \frac{4^*\pi^2}{h}|V_{ij}|^2 \frac{1}{\sqrt{4\pi\lambda_c k_B T}} \sum_n P_T(n) \sum_m \left|FCI_{nm}\left(S_{eff}\right)\right|^2 \times \exp\left[\frac{\left(\Delta G_{ij} + \lambda_c + (m-n)h\nu_{eff}\right)^2}{4\lambda_c k_B T}\right], \quad (1)$$

where h is the Planck constant, V_{ij} is the electronic coupling between the initial i and final j electronic states, λ_c is the classical

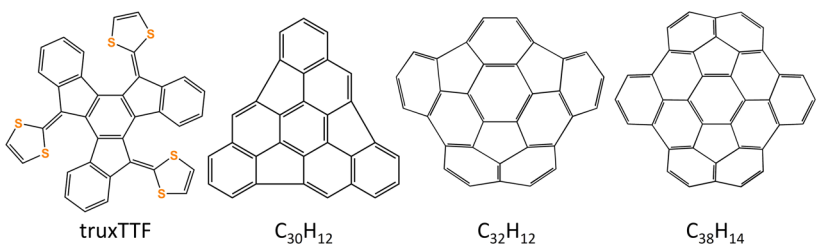

FIG. 2. Chemical structures of truxTTF, $C_{30}H_{12}$, $C_{32}H_{12}$, and $C_{38}H_{14}$.

reorganization energy including intramolecular and external (solvent) components, k_B corresponds to the Boltzmann constant, T is the temperature, $P_T(n)$ represents the Boltzmann probability that a vibrational state n on an initial electronic state i is occupied at a certain temperature, and ΔG_{ij} is the Gibbs free energy difference between the initial and final states and is approximated by the adiabatic energy difference ΔE_{ij}. Finally, the Franck–Condon (FC) integral, referred to as $FCI_{\mathrm{nm}}(S_{\mathrm{eff}})$, represents the overlap between the vibrational wavefunctions of the initial (n) and final (m) states in the electronic transition from the initial state i to the final state j.[44] The $FCI_{\mathrm{nm}}(S_{\mathrm{eff}})$ integral is influenced by the Huang–Rhys (HR) factor, denoted as S_{eff}, which characterizes the relative displacement along an effective quantum normal mode with a corresponding frequency ν_{eff}. All the details of how the different parameters entering Eq. (1) are computed can be found in Sec. S1 of the supplementary material.

Computational details

The Gaussian16 package, specifically in its revision A03,[45] was employed for all the electronic structure calculations, with the exception of the optimization of the ground-state geometries of the three supramolecular complexes: truxTTF·$C_{30}H_{12}$,[36] truxTTF·$C_{32}H_{12}$,[37] and truxTTF·$C_{38}H_{14}$.[37] These geometries were derived from previously published results at the revPBE0-D3/cc-pVTZ level. For excited-state calculations, the TD-DFT approach in its Tamm–Dancoff variant[46] (TDA-DFT) was utilized due to its lower wavefunction instabilities.[47,48] This is particularly convenient when the approach to compute the excited states is coupled to a diabatization scheme based on a wavefunction property, as in the method used in this paper (see below). The calculations employed the optimally tuned LC-BLYP[49,50] (OT-LC-BLYP) functional in combination with the Pople's 6-31G** basis set.[51] The optimal ω values within the OT-LC-BLYP density functional were calculated to be 0.15, 0.14, 0.19, and 0.16 bohr^{-1} for truxTTF, $C_{30}H_{12}$, $C_{32}H_{12}$, and $C_{38}H_{14}$, respectively (see Sec. S1.1 of the supplementary material). Solvent effects were incorporated using the polarizable continuum model (PCM)[52,53] with *o*-dichlorobenzene as the solvent. For adiabatic energies of local excited (LE)- and CT-type excited states, the energies were recalculated through single-point calculations using the state-specific PCM (SS-PCM) approach[54] after using the linear-response PCM for geometry optimization. This approach ensures an accurate consideration of the CT stabilization arising from environmental polarization and reorganization effects.

Electronic couplings (V_{ij}) were determined employing a multistate multifragment diabatization scheme[55] based on the fragment particle-hole densities (FPHD) implemented in a homemade code developed in our group. This program makes use of the overlap matrix between the atomic basis functions, the molecular orbital coefficients, and the excitation coefficients obtained from TDA-DFT calculations.

RESULTS AND DISCUSSION

Supramolecular heterodimer structures

In prior investigations, the minimum-energy supramolecular structures of the truxTTF·$C_{30}H_{12}$, truxTTF·$C_{32}H_{12}$, and truxTTF·$C_{38}H_{14}$ D–A heterodimers were examined using the revPBE0-D3/cc-pVTZ level.[36,37] This exploration revealed different configurations, characterized by either concave–concave or concave–convex intermolecular dispositions. Depending on the orientation of the truxTTF donor relative to the acceptor, short intermolecular contacts of different natures (e.g., C···S or C···C) are found, as illustrated in Figs. S5–S7. For the three complexes, the most stable structure was found to correspond to the concave–convex intermolecular orientation in which a dithiol ring from the truxTTF donor resides within the basin of the buckybowl acceptor (Fig. 3). These staggered structures exhibit enhanced stability owing to the substantial number of CH···π and π–π interactions. In addition, these structures display more favorable C···S short intermolecular contacts within the 2.5–4.0 Å range compared to their C···C counterparts.[36,56]

Electronic structure

As a first step, we analyze the electronic structure of the D–A heterodimers to rationalize how the acceptor size influences

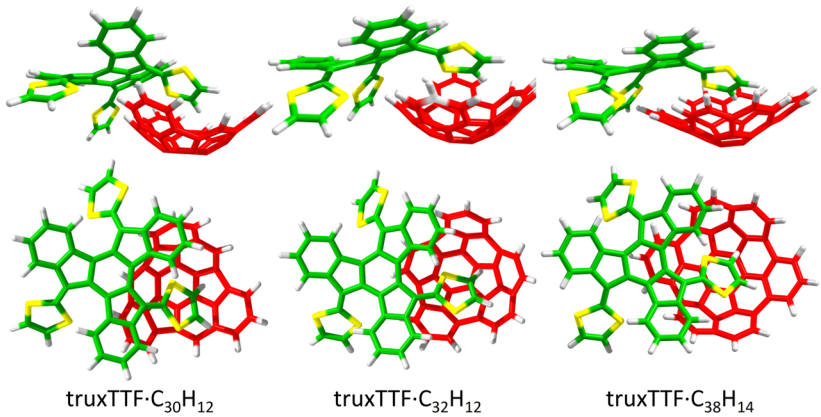

FIG. 3. Most stable staggered structures predicted for the truxTTF·$C_{30}H_{12}$, truxTTF·$C_{32}H_{12}$, and truxTTF·$C_{38}H_{14}$ supramolecular D–A heterodimers. Color code: carbon atoms in green (truxTTF) and red (buckybowls), sulfur in yellow, and hydrogen in white.

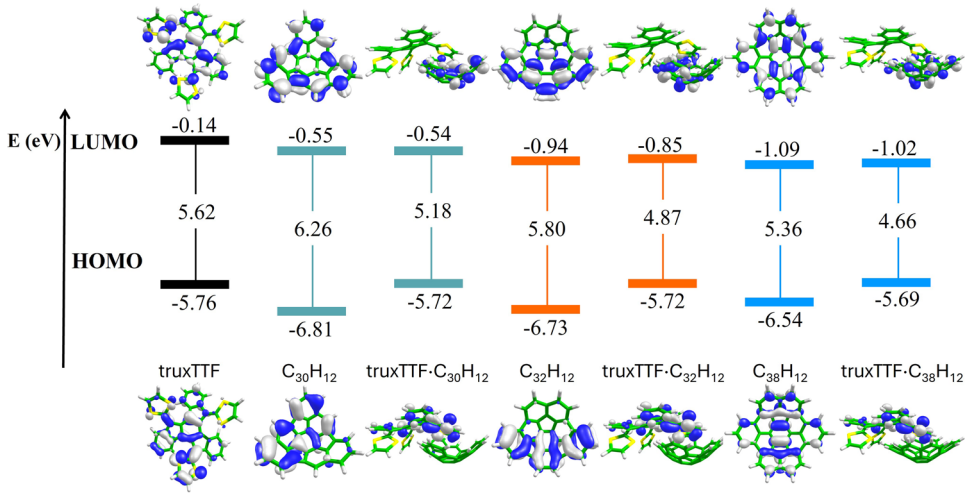

FIG. 4. HOMO and LUMO energies calculated at the LC-BLYP(ω = 0.16)/6-31G** level in *o*-dichlorobenzene for the isolated truxTTF donor and the buckybowl acceptors ($C_{30}H_{12}$, $C_{32}H_{12}$, and $C_{38}H_{14}$), as well as for the respective supramolecular heterodimers (truxTTF·$C_{30}H_{12}$, truxTTF·$C_{32}H_{12}$, and truxTTF·$C_{38}H_{14}$).

the energy levels. Ground state DFT calculations at the LC-BLYP/6-31G** level using an average ω of 0.16 have been performed for a reliable comparison. LC-BLYP computations reveal, as expected, that the highest-occupied molecular orbital (HOMO) of the three acceptors is found to be lower in energy (−6.81, −6.73, and −6.54 eV for $C_{30}H_{12}$, $C_{32}H_{12}$, and $C_{38}H_{14}$, respectively) than the HOMO computed for the donor truxTTF (−5.76 eV). This energy difference ensures that the HOMO is fully localized on the truxTTF moiety for the three D–A complexes (Fig. 4). The HOMO energies computed for the three heterodimers (−5.72, −5.72, and −5.69 eV for truxTTF·$C_{30}H_{12}$, truxTTF·$C_{32}H_{12}$, and truxTTF·$C_{38}H_{14}$, respectively) are indeed comparable to those of isolated truxTTF (−5.76 eV). The lowest-unoccupied molecular orbital (LUMO) calculated for the acceptor $C_{30}H_{12}$ (−0.55 eV), $C_{32}H_{12}$ (−0.94 eV), and $C_{38}H_{14}$ (−1.09 eV) buckybowls are lower in energy than the LUMO of truxTTF (−0.14 eV). Hence, the LUMO of the three D–A heterodimers is localized on the acceptor moiety and is computed at energies (−0.54, −0.85, and −1.02 eV for truxTTF·$C_{30}H_{12}$, truxTTF·$C_{32}H_{12}$, and truxTTF·$C_{38}H_{14}$, respectively) similar to those of the isolated acceptors. Therefore, there is a stabilization of the LUMO level when increasing the size of the buckybowl unit due to the extension of the π-conjugated system. To summarize, the three D–A complexes present similar HOMO energies localized in the donor moiety and a noticeable LUMO stabilization as the acceptor size increases. Consequently, a decrease in the HOMO–LUMO energy gap is predicted upon increasing the buckybowl size (5.18, 4.87, and 4.66 eV for truxTTF·$C_{30}H_{12}$, truxTTF·$C_{32}H_{12}$, and truxTTF·$C_{38}H_{14}$, respectively), which suggests a red-shift of the lowest excited states as a function of the acceptor size.

Excited states and electronic couplings

An important parameter necessary to evaluate the CS rates for the three heterodimers (truxTTF·$C_{30}H_{12}$, truxTTF·$C_{32}H_{12}$, and truxTTF·$C_{38}H_{14}$) is the electronic couplings (V_{ij}) between all involved excited states. In a previous study, we showed that up to six low-lying excited states of different natures [local excited (LE) and charge transfer (CT)] participated in the photoinduced CS process for the truxTTF·$C_{30}H_{12}$ dimer and that, in that context, a multistate diabatization scheme was needed to obtain accurate coupling predictions.[41] The electronic couplings are here evaluated at the Franck–Condon (FC) region (ground-state geometry of the truxTTF·$C_{30}H_{12}$ dimer), since they are lowly sensitive to internal changes of the D and A moieties, using the FPHD diabatization method.[55] This method, although slightly different from that used previously,[41] is also able to deal with multiple excited states at a fixed geometry. Therefore, in line with our previous work, the couplings V_{ij} were evaluated at the FC region of the three D–A complexes from DFT calculations using an optimally tuned long-range corrected BLYP functional (OT-LC-BYLP/6-31G** level of theory), where the ω parameter has been optimized for each individual system. Calculations were performed within the TDA-DFT approximation, including solvation effects (o-dichlorobenzene) within the polarized continuum medium (PCM) approach (see Sec. S1 in the supplementary material for further methodology details).

To explore the effect of the buckybowl size, we first analyzed the low-lying electronic excited states relevant to the CS process in the three D–A complexes. Figure 5 summarizes the values of the vertical excitation energies (ΔE), the oscillator strengths (f), and the charge difference between the donor and acceptor moieties (Δq)[57] calculated for the lowest-energy excited states potentially involved in the CS process (see Sec. 2.2 and Table S1 in the supplementary material for detailed information). The Δq value is used as a descriptor to do a first characterization of the adiabatic states as LE or CT. States with $\Delta q > 1e$ indicate a significant CT character, whereas states with $\Delta q < 1e$ are characteristic of LE excitations involving only the truxTTF donor or the buckybowl acceptor. As stated above, truxTTF·$C_{30}H_{12}$ presents six low-lying singlet excited states relevant to the CS process. Starting from the ground state (GS), three electronic transitions to these states (GS → CT_1, GS → CT_2, and GS

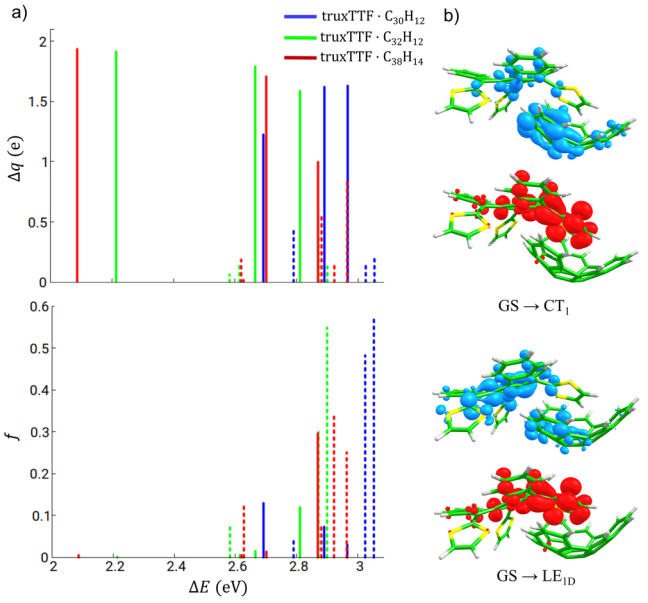

FIG. 5. (a) Representation of D–A net-charge difference (Dq, top) and oscillator strength (f, bottom) as a function of the excitation energy (ΔE) calculated for the truxTTF·$C_{30}H_{12}$, truxTTF·$C_{32}H_{12}$, and truxTTF·$C_{38}H_{14}$ complexes at the OT-LC-BLYP/6-31G** level in *o*-dichlorobenzene within the PCM approach. Solid lines represent CT states, and dashed lines represent LE states. (b) Attachment (top) and detachment (bottom) densities calculated for the GS → CT_1 and GS → LE_{1D} transitions of the truxTTF·$C_{30}H_{12}$ heterodimer.

TABLE I. Absolute electronic couplings V_{ij} (meV) between local (LE) and charge-transfer (CT) excited states calculated using the FPHD diabatization for truxTTF·$C_{30}H_{12}$, truxTTF·$C_{32}H_{12}$, and truxTTF·$C_{38}H_{14}$.

truxTTF·$C_{30}H_{12}$			
V_{ij} (meV)	CT_1	CT_2	CT_3
LE_{1D}	47.4	0.3	9.1
LE_{2D}	27.5	3.8	8.6
LE_{3D}	16.2	10.3	6.4
truxTTF·$C_{32}H_{12}$			
V_{ij} (meV)	CT_1	CT_2	CT_3
LE_{1D}	47.8	12.7	4.0
LE_{2D}	44.3	1.8	20.2
LE_{3D}	12.0	31.1	15.9
LE_{1A}	36.6	6.3	2.04
truxTTF·$C_{38}H_{14}$			
V_{ij} (meV)	CT_1	CT_2	CT_3	CT_4
LE_{1D}	14.4	23.9	18.1	9.5
LE_{2D}	29.5	19.8	19.6	29.1
LE_{3D}	13.8	29.0	29.6	11.8
LE_{1A}	53.7	7.2	0.1	28.5

→ CT_3) exhibit a significant charge transfer from the donor to the acceptor and are calculated at 2.69, 2.89, and 2.97 eV, respectively. The CT character of these transitions is corroborated by their low oscillator strengths, the Δq values (1.22, 1.62, and 1.63e for CT_1, CT_2, and CT_3, respectively), and the attachment/detachment densities calculated for all of them [Fig. 5(b), Table S1, and Fig. S11(a)]. The lowest electronic transition (GS → CT_1) does not hold a pure CT character and is rather mixed with a local excitation in the truxTTF donor, as indicated by the Δq value (1.22e) and the attachment/detachment densities [Fig. 5(b)]. In addition to the CT-type transitions, the three lowest-energy LE-type excitations (GS → LE_{1D}, GS → LE_{2D}, and GS → LE_{3D}, where D stands for the donor) localized on the truxTTF unit are predicted at 2.79, 3.02, and 3.05 eV, respectively, and show small Δq values in the 0.14–0.45e range [Fig. 5(b), Table S1 and Fig. S11(b)]. Whereas the first GS → LE_{1D} transition exhibits a small oscillator strength (f = 0.042), the GS → LE_{2D} and GS → LE_{3D} excitations correspond to bright transitions (f = 0.482 and 0.579, respectively), consistent with the electronic transitions already reported for isolated truxTTF.[36] Therefore, the photoinduced CS process is expected to be initiated in states LE_{2D} and LE_{3D} after light absorption.

Similar to truxTTF·$C_{30}H_{12}$, truxTTF·$C_{32}H_{12}$ and truxTTF·$C_{38}H_{14}$ also present a complex scenario with several LE- and CT-type states below or close in energy to the bright states [Fig. 5(a) and Table S1]. The low-lying CT excitations (GS → CT_1, GS → CT_2, and GS → CT_3) are in general predicted at lower energies than those found for truxTTF·$C_{30}H_{12}$, especially for the lowest-energy GS → CT_1. This is in line with the smaller HOMO–LUMO energy gap computed for truxTTF·$C_{32}H_{12}$ and truxTTF·$C_{38}H_{14}$. Unlike truxTTF·$C_{30}H_{12}$, the increase in the acceptor size causes the appearance of a new LE excitation (GS → LE_{1A}, where A stands for the acceptor) localized on the bucky-bowl with a small f. This opens the energy transfer (ET) between the D and A units as a new pathway to consider before the CS process can occur (see Fig. 1). It should be noted that for truxTTF·$C_{38}H_{14}$, the description of the low-lying excited states in terms of LE- or CT-type character is more complex due to the significant mixing, as indicated by the Δq values and the attachment/detachment densities (Table S1 and Figs. S12 and S13).

Tables I and S2 gather the electronic couplings (V_{ij}) calculated between all the low-lying singlet excited states for the three truxTTF·$C_{30}H_{12}$, truxTTF·$C_{32}H_{12}$, and truxTTF·$C_{38}H_{14}$ supramolecular complexes. These couplings, computed with the FPHD-based method, are in good agreement with those obtained using the multistate multi-FED-FCD (FED: fragment exciton difference and FCD: fragment charge difference) diabatization scheme[58–60] (Table S3). Note that there are only a few multistate methods able to diabatize simultaneously LE and CT states, the multi-FED-FCD scheme being the first one (as far as we know) reported in 2018. As there is not a unique set of diabatic states, which are extremely dependent on the chosen property to find the adiabatic-to-diabatic rotation matrix, the good agreement between both schemes, FPHD and multi-FED-FCD, shows the robustness of both diabatization processes.

As previously discussed,[41] truxTTF·$C_{30}H_{12}$ displays values of V_{ij} in the 0–47 meV range, with the highest couplings corresponding to those between the LE states with the lowest-energy CT (47.4, 27.5, and 16.2 meV for $V_{LE1D\text{-}CT1}$, $V_{LE2D\text{-}CT1}$, and $V_{LE3D\text{-}CT1}$, respectively). These V_{ij} values are consistent with the nature of the CT_1 state with a non-negligible mixing with LE excitations, as suggested by the value of Δq [1.22, Fig. 5(a)] and the attachment/detachment densities [Figs. 5(b) and S11]. Whereas this trend is mainly preserved for truxTTF·$C_{32}H_{12}$, truxTTF·$C_{38}H_{14}$ displays significant electronic couplings (>10 meV) between almost all the excited states. For truxTTF·$C_{32}H_{12}$ and truxTTF·$C_{38}H_{14}$, the excitonic interactions between the LE-type states localized on the D and A units give rise to small couplings in the 0.1–8.0 meV range (Table S2), with higher values being found for truxTTF·$C_{38}H_{14}$. Therefore, the truxTTF·$C_{38}H_{14}$ heterodimer with the largest buckybowl holds moderate/high excitonic/electronic couplings, which may promote multiple ET and CT processes before the ultimate CS according to the coupling V_{ij} values.

Gibbs free energy difference and reorganization energy

To estimate the electron- and/or energy-transfer rate constants using the MLJ rate expression [Eq. (1) in the Methodology Section], the Gibbs free energy difference (ΔG) between the initial and final electronic states and the reorganization energy (λ) have to be computed. In line with previous works,[41,61] ΔG is approximated to the adiabatic energy difference (ΔE) between the respective electronic states. In a rigorous manner, the calculation of ΔE would imply the geometry optimization of all the singlet excited states involved in the transfer process, which becomes unaffordable by using the TDA-DFT approach due to the energy proximity and similar nature of the relevant excited states. Instead, and based on our previous work,[41] we have used the optimized structure calculated for the lowest-energy CT state of the respective heterodimer and that computed for the lowest-energy LE state of the isolated D and A units to estimate the adiabatic energies of all involved excited states. In addition, the energies were corrected using the state-specific PCM (SS-PCM) approach, which is more accurate in capturing the stabilization of each excited state by solvent effects, especially for CT-type states (see Sec. S2.4 in the supplementary material for additional details).

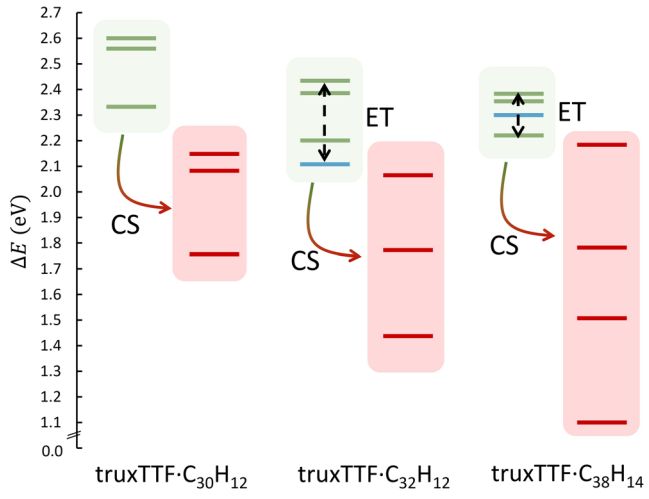

FIG. 6. Schematic diagram showing the adiabatic energy differences (ΔE), computed within the TDA-DFT/SS-PCM approach for the lowest-energy CT (in red) and LE (in green/blue for donor/acceptor) excited states of truxTTF·$C_{30}H_{12}$, truxTTF·$C_{32}H_{12}$, and truxTTF·$C_{38}H_{14}$. Energy-transfer (ET) and charge-separation (CS) processes are indicated.

Figure 6 displays the adiabatic energy differences, relative to the electronic ground state, estimated for all the relevant excited states of the truxTTF·$C_{30}H_{12}$, truxTTF·$C_{32}H_{12}$, and truxTTF·$C_{38}H_{14}$ complexes (see Table S4 for the ΔE values). For the three heterodimers, the CT states are lower in energy than the LE states upon considering the solvent effects within the SS-PCM approach. Nevertheless, significant differences between the three heterodimers are found. Whereas for truxTTF·$C_{30}H_{12}$, bearing the smallest buckybowl, the CT states below the LE states are concentrated in a range of values lower than 0.4 eV, the CT states of truxTTF·$C_{32}H_{12}$ and truxTTF·$C_{38}H_{14}$ spread over a range of around 0.6 and 1.1 eV, respectively (Fig. 6 and Table S4).

Regarding the reorganization energy, the MLJ rate expression [Eq. (1)] includes a classical reorganization energy (λ_c) associated with the electron-transfer reaction (intramolecular and solvent degrees of freedom) and incorporates quantum effects (e.g., tunneling) through an effective vibration (see Sec. S1.4 for full details). For the CS process (starting from LE_D states of the truxTTF), similar λ_c values were estimated for the three truxTTF·$C_{30}H_{12}$, truxTTF·$C_{32}H_{12}$, and truxTTF·$C_{38}H_{14}$ complexes (1.07, 1.15, and 1.05 eV, respectively). For truxTTF·$C_{32}H_{12}$ and truxTTF·$C_{38}H_{14}$, the λ_c values inferred for the CS pathways from the LE_A state localized

TABLE II. Relevant parameters (V_{ij}, ΔG, and λ_c in eV, υ_{eff} in cm^{-1} and S_{eff}) and estimated rate constants (k in s^{-1}) for the most relevant charge-separation pathways in the truxTTF·$C_{30}H_{12}$, truxTTF·$C_{32}H_{12}$, and truxTTF·$C_{38}H_{14}$ heterodimers.

Transition	ΔG	λ_c	V_{ij}	υ_{eff}	S_{eff}	k
truxTTF·$C_{30}H_{12}$						
$LE_{1D} \rightarrow CT_1$	−0.576	1.07	0.047	690	3.12	1.2×10^{12}
$LE_{2D} \rightarrow CT_1$	−0.803	1.07	0.027	690	3.12	2.9×10^{12}
$LE_{3D} \rightarrow CT_1$	−0.830	1.07	0.016	690	3.12	1.3×10^{12}
truxTTF·$C_{32}H_{12}$						
$LE_{1D} \rightarrow CT_1$	−0.763	1.15	0.048	705	3.77	2.8×10^{12}
$LE_{2D} \rightarrow CT_1$	−0.948	1.15	0.043	705	3.77	9.3×10^{12}
$LE_{3D} \rightarrow CT_2$	−0.661	1.15	0.045	705	3.77	9.3×10^{11}
$LE_{1A} \rightarrow CT_1$	−0.670	1.48	0.037	741	1.77	1.5×10^{11}
truxTTF·$C_{38}H_{14}$						
$LE_{1D} \rightarrow CT_1$	−1.129	1.05	0.014	630	3.36	4.1×10^{12}
$LE_{1D} \rightarrow CT_2$	−0.713	1.05	0.024	630	3.36	1.3×10^{12}
$LE_{2D} \rightarrow CT_1$	−1.263	1.05	0.030	630	3.36	2.3×10^{13}
$LE_{2D} \rightarrow CT_2$	−0.846	1.05	0.020	630	3.36	2.5×10^{12}
$LE_{3D} \rightarrow CT_1$	−1.292	1.05	0.015	630	3.36	5.7×10^{12}
$LE_{3D} \rightarrow CT_2$	−0.875	1.05	0.029	630	3.36	6.2×10^{12}
$LE_{1A} \rightarrow CT_1$	−1.208	1.41	0.005	663	1.41	3.9×10^{13}

on the buckybowl were also found to be similar (1.48 and 1.41 eV, respectively). As λ_c has similar values for the three heterodimers, the difference in the rate constants will be more determined by the couplings and effective vibrations, but especially by the adiabatic ΔE offset, which covers a wider range of energies as the acceptor size increases (see Sec. S2.5 in the supplementary material for further discussion).

Charge-separation (k_{CS}) and energy-transfer (k_{ET}) rate constants and kinetic model

After the collection and discussion of the parameters needed to estimate the MLJ rates [Eq. (1)], the rate constants for the different charge-separation (k_{CS}) and energy-transfer (k_{ET}) pathways were evaluated for the three supramolecular heterodimers (Tables II and S8–S10). Figure 7(a) shows a schematic picture of the kinetic relevance of the different CS channels for the three complexes. For truxTTF·$C_{30}H_{12}$, the CS process is found to be fast from any of the LE_D excited states (LE_{1D}, LE_{2D}, and LE_{3D}) to the lowest-energy CT_1 state. The rate constants calculated for these $LE_D \rightarrow CT_1$ processes are in the 1.2–2.9 × 10^{12} s^{-1} range (Tables II and S8), in good accord with the reported experimental rate (6.6 × 10^{11} s^{-1}).[36] It is likely that the most prominent CS pathway results from the $LE_{1D} \rightarrow CT_1$ channel after an internal conversion (generally ultrafast) from the bright LE_{2D} and LE_{3D} states to LE_{1D}. Similar to truxTTF·$C_{30}H_{12}$, the fastest CS rates calculated for truxTTF·$C_{32}H_{12}$ are associated with the $LE_{1D} \rightarrow CT_1$ and $LE_{2D} \rightarrow CT_1$ electron-transfer pathways with rates of 2.8 and 9.3 × 10^{12} s^{-1}, respectively (Tables II and S9). Similarly, a secondary efficient CS channel involving a hot CT state ($LE_{3D} \rightarrow CT_2$) was also found (9.3 × 10^{11} s^{-1}). Interestingly, the LE_A-type excited state, localized on the buckybowl and absent in truxTTF·$C_{30}H_{12}$, also gives rise to a relatively fast CS process via a $LE_{1A} \rightarrow CT_1$ transition with a rate of 1.5 × 10^{11} s^{-1}. Nevertheless, the possibility of a fast energy transfer between the LE_D and LE_A states before the CS event is unlikely according to the ET rates, which are several orders of magnitude smaller than those computed for a direct CS (Tables II and S9). Unlike truxTTF·$C_{30}H_{12}$ and truxTTF·$C_{32}H_{12}$, the CS process for truxTTF·$C_{38}H_{14}$ (the complex with the largest buckybowl acceptor) can occur more efficiently through multiple transitions with fast k_{CS} constants in the 1.3 × 10^{12}–3.9 × 10^{13} s^{-1} range (Tables II and S10). This is in line with the experimental timescale for the CS event (0.8 ps, 1.3 × 10^{12} s^{-1}).[37] Interestingly, the $LE_{1A} \rightarrow CT_1$ pathway, starting from an excitation localized on the buckybowl, is obtained to be the most efficient channel (3.9 × 10^{13} s^{-1}). However, this pathway is not expected to be the dominant one since the LE_D excitations centered on the truxTTF moiety exhibit higher oscillator strengths, and the k_{ET} constants calculated for the D → A ET processes are significantly slower than those predicted for the $LE_D \rightarrow CT$ CS processes (e.g., 2.5 × 10^9 and 3.2 × 10^9 s^{-1} for $LE_{2D} \rightarrow LE_{1A}$ and $LE_{3D} \rightarrow LE_{1A}$, respectively, Table S10).

To obtain a global picture of the CS event, a simple kinetic model including all the previously computed k_{CS} and k_{ET} rate constants was built up for truxTTF·$C_{30}H_{12}$, truxTTF·$C_{32}H_{12}$, and

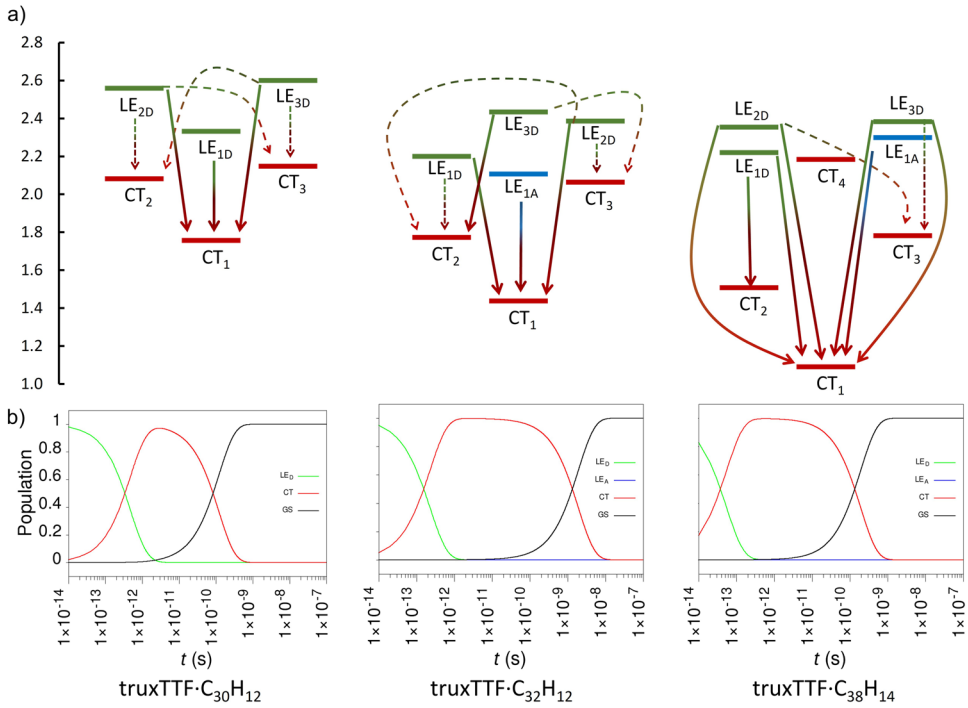

FIG. 7. (a) Scheme representing the CS and ET pathways for truxTTF·$C_{30}H_{12}$ (left), truxTTF·$C_{32}H_{12}$ (center), and truxTTF·$C_{38}H_{14}$ (right) complexes. The thickness of the arrows indicates the relevance of the decay channels, according to Tables S8–S10. (b) Time evolution of the population of the different electronic states according to their nature (CT, LE_D, LE_A, and GS) calculated for the three complexes according to the kinetic model proposed (see Sec. S3 in the supplementary material for further details). Time (*x*-axis) is represented on a logarithmic scale.

truxTTF·$C_{38}H_{14}$ (see Sec. S3 in the supplementary material for further details). Figure 7(b) displays the time evolution of the populations of the different electronic states according to their nature (LE_D, LE_A, CT, and GS) calculated for the three D–A complexes, whereas Fig. S17 shows the population of each excited state as a function of time. In a broad perspective, the kinetic model shows that the photoinduced CS process, estimated from the 50% increase in population of the CT states, occurs in the sub-ps timescale (0.3, 0.2, and 0.035 ps for truxTTF·$C_{30}H_{12}$, truxTTF·$C_{32}H_{12}$, and truxTTF·$C_{38}H_{14}$, respectively). The reciprocal of these half-life times provides global k_{CS} values of 3.3×10^{12}, 5.0×10^{12}, and 2.9×10^{13} s^{-1} for truxTTF·$C_{30}H_{12}$, truxTTF·$C_{32}H_{12}$, and truxTTF·$C_{38}H_{14}$, respectively, that nicely reproduce the higher decay rate constant experimentally reported for truxTTF·$C_{38}H_{14}$ (3.3×10^{12} s^{-1}) compared with truxTTF·$C_{30}H_{12}$ (6.6×10^{11} s^{-1}) and truxTTF·$C_{32}H_{12}$ (6.3×10^{11} s^{-1}). A more detailed analysis (Fig. S17) reveals that the main CS mechanism for the three heterodimers results from electronic transitions from LE_D states (centered on truxTTF) to the lowest-energy CT_1, in accordance with the high population of this CT state until its decay to the ground state (recombination). Nevertheless, for truxTTF·$C_{32}H_{12}$ and truxTTF·$C_{38}H_{14}$, bearing more extended buckybowls, CS can also occur via hot CT states (as a secondary route) with small but non-negligible populations of CT_2 and CT_3.

Overall, our findings suggest that the buckybowl size influences the efficiency of the global photoinduced CS process. In particular, CS becomes more efficient as the backbone of the buckybowl acceptor becomes more extended. Therefore, truxTTF·$C_{38}H_{14}$ exhibits the fastest CS event (approximately ten times faster than that estimated for truxTTF·$C_{30}H_{12}$ and truxTTF·$C_{32}H_{12}$), in line with the multiple and efficient CS channels discussed above. However, it should be noted that the final CS rate results from a very subtle balance between many parameters, and no linear dependency between size and CS efficiency has to be expected. The energy of the CT states will decrease for larger buckybowls, thus increasing the ΔE_{LE-CT} difference that will be optimal to reach the resonance condition with the reorganization energy ($\Delta E_{LE-CT} + \lambda = 0$). In addition, larger curvatures will be translated into different supramolecular arrangements that may affect the electronic couplings in an unpredictable way. In contrast, the moderate differences between the buckybowls investigated here and the similar structural arrangements displayed by the supramolecular D–A complexes they form with truxTTF make the size of the acceptor a key parameter in determining the differences found in the CS efficiency.

CONCLUSION

In this work, we have gained theoretical insight into the photoinduced process (charge separation and energy transfer) within a family of donor–acceptor supramolecular complexes, where the electron-acceptor units are buckybowl systems of increasing size ($C_{30}H_{12}$, $C_{32}H_{12}$, and $C_{38}H_{14}$) and the electron-donor fragment is the truxene-tetrathiafulvalene (truxTTF) molecule. To estimate the charge-separation rate constants of the truxTTF·$C_{30}H_{12}$, truxTTF·$C_{32}H_{12}$, and truxTTF·$C_{38}H_{14}$ supramolecular heterodimers, we have adopted a theoretical approach combining electronic structure calculations performed at the (time-dependent) DFT level, a multistate multifragment diabatization method, the Marcus–Levitch–Jortner (MLJ) semiclassical rate expression, and a simple kinetic model. Our outcomes highlight that even a moderate modification in the buckybowl size impacts largely the photoinduced charge separation event, making this process more efficient as the size of the buckybowl grows among the acceptor series here studied. The truxTTF·$C_{38}H_{14}$ complex (bearing the largest buckybowl) exhibits multiple and efficient electron-transfer channels, providing a global photoinduced charge separation in the ultrafast sub-ps timescale in good agreement with the reported experimental findings. This work, therefore, points out that the proper tuning and control of the buckybowl molecular shape and size can be seen as an attractive approach for novel acceptors that, combined with proper electron-donor systems, may give rise to efficient photoinduced charge separation, which is interesting for potential photovoltaic applications.

SUPPLEMENTARY MATERIAL

See the supplementary material for detailed information about the theoretical protocol employed and additional data and figures.

ACKNOWLEDGMENTS

The financial support by the MCIN/AEI of Spain (Project Nos. CNS2022-135187, PID2021-128569NB-I00, PID2020-119748GA-I00, and TED2021-131255B-C44, funded by MCIN/AEI/10.13039/501100011033, "ERDF A way of making Europe," and "European Union NextGeneration EU/PRTR") and the Generalitat Valenciana (Grant No. MFA/2022/017) is acknowledged. Grant No. MFA/2022/017 project forms part of the Advanced Materials program supported by MCIN with funding from European Union NextGenerationEU (PRTR-C17.I1) and by Generalitat Valenciana. R.R.-A. acknowledges Grant No. PRE2019-089226 funded by MCIN/AEI/10.13039/501100011033 and "ESF Investing in your future." J.C. thanks to the European Union for its Marie Curie Individual Fellowship (HORIZON-MSCA-2022-PF-01-01, Project No. 101106941).

AUTHOR DECLARATIONS

Conflict of Interest

The authors have no conflicts to disclose.

Author Contributions

R.R.-A. and J.C. contributed equally to this work.

Raquel Rubert-Albiol: Conceptualization (equal); Formal analysis (equal); Investigation (equal); Methodology (equal); Writing – original draft (lead). **Jesús Cerdá**: Conceptualization (equal); Formal analysis (equal); Investigation (equal); Methodology (equal); Software (equal); Writing – original draft (lead). **Joaquín Calbo**: Investigation (supporting); Writing – review & editing (supporting). **Lorenzo Cupellini**: Software (supporting). **Enrique Ortí**: Funding

acquisition (lead); Project administration (lead); Resources (lead); Supervision (lead); Writing – review & editing (lead). **Juan Aragó**: Conceptualization (lead); Funding acquisition (lead); Investigation (lead); Methodology (lead); Project administration (lead); Resources (lead); Supervision (lead); Writing – review & editing (lead).

DATA AVAILABILITY

The data that support the findings of this study are available from the corresponding authors upon reasonable request.

REFERENCES

[1] M. Natali, S. Campagna, and F. Scandola, "Photoinduced electron transfer across molecular bridges: Electron- and hole-transfer superexchange pathways," Chem. Soc. Rev. **43**(12), 4005–4018 (2014).

[2] R. C. Dorfman, M. Tachiya, and M. D. Fayer, "Forward and back photoinduced electron transfer in solid solutions: A comparison of theoretical methods," Chem. Phys. Lett. **179**(1–2), 152–158 (1991).

[3] O. A. Stasyuk, A. A. Voityuk, A. J. Stasyuk, and M. Sola, "Photoinduced electron transfer in inclusion complexes of carbon nanohoops," Acc. Chem. Res. **57**, 37–46 (2024).

[4] D. Escudero, "Revising intramolecular photoinduced electron transfer (PET) from first-principles," Acc. Chem. Res. **49**, 1816–1824 (2016).

[5] C. Deibel, T. Strobel, and V. Dyakonov, "Role of the charge transfer state in organic donor–acceptor solar cells," Adv. Mater. **22**(37), 4097–4111 (2010).

[6] W. Sun, M. Li, J. Fan, and X. Peng, "Activity-based sensing and theranostic probes based on photoinduced electron transfer," Acc. Chem. Res. **52**, 2818–2831 (2019).

[7] B. Daly, J. Ling, and A. P. de Silva, "Current developments in fluorescent PET (photoinduced electron transfer) sensors and switches," Chem. Soc. Rev. **44**(13), 4203–4211 (2015).

[8] H. Duan, F. Cao, H. Hao, H. Bian, and L. Cao, "Efficient photoinduced energy and electron transfers in a tetraphenylethene-based octacationic cage through host-guest complexation," ACS Appl. Mater. Interfaces **13**(14), 16837–16845 (2021).

[9] S. Fukuzumi, K. Ohkubo, and T. Suenobu, "Long-lived charge separation and applications in artificial photosynthesis," Acc. Chem. Res. **47**, 1455–1464 (2014).

[10] L. Hammarström, "Accumulative charge separation for solar fuels production: Coupling light-induced single electron transfer to multielectron catalysis," Acc. Chem. Res. **48**(3), 840–850 (2015).

[11] A. M. Ramos, M. T. Rispens, J. K. J. van Duren, J. C. Hummelen, and R. A. J. Janssen, "Photoinduced electron transfer and photovoltaic devices of a conjugated polymer with pendant fullerenes," J. Am. Chem. Soc. **123**(27), 6714–6715 (2001).

[12] M. Grätzel, "Dye-sensitized solar cells," J. Photochem. Photobiol., C **4**(2), 145–153 (2003).

[13] A. Alesadi, W. Xia, and D. Kilin, "Photo-induced charge transfer of fullerene and non-fullerene conjugated polymer blends via ab initio excited-state dynamics," J. Phys. Chem. C **126**(29), 12015–12024 (2022).

[14] Z. Chen and H. Zhu, "Photoinduced charge transfer and recombination dynamics in star nonfullerene organic solar cells," J. Phys. Chem. Lett. **13**(4), 1123–1130 (2022).

[15] X. Y. Zhu, Q. Yang, and M. Muntwiler, "Charge-transfer excitons at organic semiconductor surfaces and interfaces," Acc. Chem. Res. **42**(11), 1779–1787 (2009).

[16] G. Chidichimo and L. Filippelli, "Organic solar cells: Problems and perspectives," Int. J. Photoenergy **2010**, 123534.

[17] W. Cao and J. Xue, "Recent progress in organic photovoltaics: Device architecture and optical design," Energy Environ. Sci. **7**(7), 2123–2144 (2014).

[18] C. J. Brabec, S. Gowrisanker, J. J. M. Halls *et al.*, "Polymer–fullerene bulk-heterojunction solar cells," Adv. Mater. **22**, 3839–3856 (2010).

[19] C. Deibel and V. Dyakonov, "Polymer–fullerene bulk heterojunction solar cells," Rep. Prog. Phys. **73**(9), 096401 (2010).

[20] G. Li, V. Shrotriya, J. Huang, Y. Yao, T. Moriarty, K. Emery, and Y. Yang, "High-efficiency solution processable polymer photovoltaic cells by self-organization of polymer blends," Nat. Mater. **4**(11), 864–868 (2005).

[21] H. Ohkita, S. Cook, Y. Astuti, W. Duffy, S. Tierney, W. Zhang, M. Heeney, I. McCulloch, J. Nelson, D. D. C. Bradley, and J. R. Durrant, "Charge carrier formation in polythiophene/fullerene blend films studied by transient absorption spectroscopy," J. Am. Chem. Soc. **130**(10), 3030–3042 (2008).

[22] C. Groves, O. G. Reid, and D. S. Ginger, "Heterogeneity in polymer solar cells: Local morphology and performance in organic photovoltaics studied with scanning probe microscopy," Acc. Chem. Res. **43**(5), 612–620 (2010).

[23] R. D. Kennedy, A. L. Ayzner, D. D. Wanger, C. T. Day, M. Halim, S. I. Khan, S. H. Tolbert, B. J. Schwartz, and Y. Rubin, "Self-assembling fullerenes for improved bulk-heterojunction photovoltaic devices," J. Am. Chem. Soc. **130**(51), 17290–17292 (2008).

[24] R. Volpi and M. Linares, "Study of the cold charge transfer state separation at the TQ1/PC_{71}BM interface," J. Comput. Chem. **38**(14), 1039–1048 (2017).

[25] S. Karuthedath, J. Gorenflot, A. Melianas, Z. Kan, M. Kemerink, and F. Laquai, "Buildup of triplet-state population in operating TQ1:PC_{71}BM devices does not limit their performance," J. Phys. Chem. Lett. **11**(8), 2838–2845 (2020).

[26] D. Luo, W. Jang, D. D. Babu, M. S. Kim, D. H. Wang, and A. K. K. Kyaw, "Recent progress in organic solar cells based on non-fullerene acceptors: Materials to devices," J. Mater. Chem. A **10**(7), 3255–3295 (2022).

[27] C. B. Nielsen, S. Holliday, H. Y. Chen, S. J. Cryer, and I. McCulloch, "Non-fullerene electron acceptors for use in organic solar cells," Acc. Chem. Res. **48**(11), 2803–2812 (2015).

[28] H. Yao, Y. Cui, D. Qian, C. S. Ponseca, A. Honarfar, Y. Xu, J. Xin, Z. Chen, L. Hong, B. Gao, R. Yu, Y. Zu, W. Ma, P. Chabera, T. Pullerits, A. Yartsev, F. Gao, and J. Hou, "14.7% efficiency organic photovoltaic cells enabled by active materials with a large electrostatic potential difference," J. Am. Chem. Soc. **141**(19), 7743–7750 (2019).

[29] S. Haseena and M. K. Ravva, "Application of newly designed Y-series non-fullerene acceptors for high-efficient organic solar cells," Adv. Theory Simul. **6**, 2200898 (2023).

[30] P. A. Denis, "Theoretical investigation of the stacking interactions between curved conjugated systems and their interaction with fullerenes," Chem. Phys. Lett. **516**(1–3), 82–87 (2011).

[31] P. A. Denis, "Theoretical characterization of existing and new fullerene receptors," RSC Adv. **3**(47), 25296–25305 (2013).

[32] A. C. Whalley, K. N. Plunkett, A. A. Gorodetsky, C. L. Schenck, C. Y. Chiu, M. L. Steigerwald, and C. Nuckolls, "Bending contorted hexabenzocoronene into a bowl," Chem. Sci. **2**(1), 132–135 (2011).

[33] C. Y. Chiu, B. Kim, A. A. Gorodetsky, W. Sattler, S. Wei, A. Sattler, M. Steigerwald, and C. Nuckolls, "Shape-shifting in contorted dibenzotetrathienocoronenes," Chem. Sci. **2**(8), 1480–1486 (2011).

[34] G. Casella and G. Saielli, "DFT study of the interaction free energy of π-π complexes of fullerenes with buckybowls and viologen dimers," New J. Chem. **35**(7), 1453–1459 (2011).

[35] E. M. Pérez, M. Sierra, L. Sánchez, M. R. Torres, R. Viruela, P. M. Viruela, E. Ortí, and N. Martín, "Concave tetrathiafulvalene-type donors as supramolecular partners for fullerenes," Angew. Chem., Int. Ed. **46**, 1847–1851 (2007).

[36] M. Gallego, J. Calbo, J. Aragó, R. M. Krick Calderon, F. H. Liquido, T. Iwamoto, A. K. Greene, E. A. Jackson, E. M. Pérez, E. Ortí, D. M. Guldi, L. T. Scott, and N. Martín, "Electron transfer in a supramolecular associathinene fragment," Angew. Chem., Int. Ed. **53**(8), 2170–2175 (2014).

[37] M. Gallego, J. Calbo, R. M. Krick Calderon, P. Pla, Y.-C. Hsieh, E. M. Pérez, Y.-T. Wu, E. Ortí, D. M. Guldi, and N. Martín, "Complexation and electronic communication between corannulene-based buckybowls and a curved truxene-TTF donor," Chem. Eur. J. **23**, 3666–3673 (2017).

[38] S. Hagen, M. S. Bratcher, M. S. Erickson, G. Zimmermann, and L. T. Scott, "Novel syntheses of three $C_{30}H_{12}$ bowl-shaped polycyclic aromatic hydrocarbons," Angew. Chem., Int. Ed. **36**, 406–408 (1997).

[39] M.-K. Chen, H.-J. Hsin, T.-C. Wu, B.-Y. Kang, Y.-W. Lee, M.-Y. Kuo, and Y.-T. Wu, "Highly curved bowl-shaped fragments of fullerenes: Synthesis, structural analysis, and physical properties," Chem. Eur. J. **20**, 598–608 (2014).

[40]T.-C. Wu, M.-K. Chen, Y.-W. Lee, M.-Y. Kuo, and Y.-T. Wu, "Bowl-shaped fragments of C_{70} or higher fullerenes: Synthesis structural analysis and inversion dynamics," Angew. Chem., Int. Ed. **52**, 1289–1293 (2013).
[41]J. Cerdá, J. Calbo, E. Ortí, and J. Aragó, "Charge-separation and charge-recombination rate constants in a donor–acceptor buckybowl-based supramolecular complex: Multistate and solvent effects," J. Phys. Chem. A **125**(46), 9982–9994 (2021).
[42]E. R. Heller and J. O. Richardson, "Semiclassical instanton formulation of Marcus-Levich-Jortner theory," J. Chem. Phys. **152**(24), 244117 (2020).
[43]V. Stehr, R. F. Fink, M. Tafipolski, C. Deibel, and B. Engels, "Comparison of different rate constant expressions for the prediction of charge and energy transport in oligoacenes," Wiley Interdiscip. Rev.: Comput. Mol. Sci. **6**(6), 694–720 (2016).
[44]V. May and O. Khün, *Charge and Energy Transfer Dynamics in Molecular Systems* (Wiley-VCH Verlag, Weinheim, Germany, 2011).
[45]M. J. Frisch, G. W. Trucks, H. B. Schlegel, G. E. Scuseria, M. A. Robb, J. R. Cheeseman, G. Scalmani, V. Barone, G. A. Petersson, H. Nakatsuji, X. Li, M. Caricato, A. V. Marenich, J. Bloino, B. G. Janesko, R. Gomperts, B. Mennucci, H. P. Hratchian, J. V. Ortiz, A. F. Izmalov, J. L. Sonnenberg, D. Williams-Young, F. Ding, F. Lipparini, F. Egidi, J. Goings, B. Peng, A. Petrone, T. Henderson, D. Ranasinghe, V. G. Zakrzewski, J. Gao, N. Rega, G. Zheng, W. Liang, M. Hada, M. Ehara, K. Toyota, R. Fukuda, J. Hasegawa, M. Ishida, T. Nakajima, Y. Honda, O. Kitao, H. Nakai, T. Vreven, K. Throsell, J. Montgomery, Jr., J. E. Peralta, F. Ogliaro, M. J. Beapark, J. J. Heyd, E. N. Brothers, K. N. Kudin, V. N. Staroverov, T. A. Keith, R. Kobayash, J. Normand, K. Raghavachari, A. P. Rendell, J. C. Burant, S. S. Iyengar, J. Tomasi, M. Cossi, J. M. Millam, M. Klene, C. Adamo, R. Cammi, J. W. Ochterski, R. L. Martin, K. Morokuma, O. Farkas, J. B. Foresman, and D. J. Fox, Gaussian 16, Gaussian, Inc., Wallingford, CT, 2016.
[46]S. Hirata and M. Head-gordon, "Time-dependent density functional theory within the Tamm–Dancoff approximation," Chem. Phys. Lett. **314**, 291–299 (1999).
[47]J. S. Sears, T. Koerzdoerfer, C. R. Zhang, and J. L. Brédas, "Communication: Orbital instabilities and triplet states from time-dependent density functional theory and long-range corrected functionals," J. Chem. Phys. **135**(15), 151103 (2011).
[48]M. J. G. Peach, M. J. Williamson, and D. J. Tozer, "Influence of triplet instabilities in TDDFT," J. Chem. Theory Comput. **7**(11), 3578–3585 (2011).
[49]H. Iikura, T. Tsuneda, T. Yanai, and K. Hirao, "A long-range correction scheme for generalized-gradient-approximation exchange functionals," J. Chem. Phys. **115**(8), 3540–3544 (2001).
[50]T. Tsuneda and K. Hirao, "Long-range correction for density functional theory," Wiley Interdiscip. Rev.: Comput. Mol. Sci. **4**(4), 375–390 (2014).
[51]M. M. Francl, W. J. Pietro, W. J. Hehre, J. S. Binkley, M. S. Gordon, D. J. DeFrees, and J. A. Pople, "Self-consistent molecular orbital methods. XXIII. A polarization-type basis set for second-row elements," J. Chem. Phys. **77**(7), 3654–3665 (1982).
[52]J. Tomasi, B. Mennucci, and R. Cammi, "Quantum mechanical continuum solvation models," Chem. Rev. **105**(8), 2999–3094 (2005).
[53]J. Tomasi and M. Persico, "Molecular interactions in solution: An overview of methods based on continuous distributions of the solvent," Chem. Rev. **94**(7), 2027–2094 (1994).
[54]R. Improta, V. Barone, G. Scalmani, and M. J. Frisch, "A state-specific polarizable continuum model time dependent density functional theory method for excited state calculations in solution," J. Chem. Phys. **125**(5), 054103 (2006).
[55]Y. C. Wang, S. Feng, W. Liang, and Y. Zhao, "Electronic couplings for photoinduced charge transfer and excitation energy transfer based on fragment particle-hole densities," J. Phys. Chem. Lett. **12**(3), 1032–1039 (2021).
[56]J. Calbo, J. C. Sancho-García, E. Ortí, and J. Aragó, "Quantum-chemical insights into the self-assembly of carbon-based supramolecular complexes," Molecules **23**(1), 118 (2018).
[57]A. A. Voityuk, "Electronic couplings for photoinduced electron transfer and excitation energy transfer computed using excited states of noninteracting molecules," J. Phys. Chem. A **121**, 5414–5419 (2017).
[58]L. Cupellini, S. Giannini, and B. Mennucci, "Electron and excitation energy transfers in covalently linked donor-acceptor dyads: Mechanisms and dynamics revealed using quantum chemistry," Phys. Chem. Chem. Phys. **20**(1), 395–403 (2018).
[59]M. Nottoli, S. Jurinovich, L. Cupellini, A. T. Gardiner, R. Cogdell, and B. Mennucci, "The role of charge-transfer states in the spectral tuning of antenna complexes of purple bacteria," Photosynth. Res. **137**(2), 215–226 (2018).
[60]J. Tölle, L. Cupellini, B. Mennucci, and J. Neugebauer, "Electronic couplings for photo-induced processes from subsystem time-dependent density-functional theory: The role of the diabatization," J. Chem. Phys. **153**(18), 18113 (2020).
[61]T. Liu and A. Troisi, "Absolute rate of charge separation and recombination in a molecular model of the P3HT/PCBM interface," J. Phys. Chem. C **115**(5), 2406–2415 (2011).